

Pd-Pt Bimetallic Nanodendrites with High Activity for Oxygen Reduction

Byungkwon Lim,¹ Majjong Jiang,² Pedro H. C. Camargo,¹ Eun Chul Cho,¹ Jing Tao,³ Xianmao Lu,¹ Yimei Zhu,³ Younan Xia^{1*}

Controlling the morphology of Pt nanostructures can provide a great opportunity to improve their catalytic properties and increase their activity on a mass basis. We synthesized Pd-Pt bimetallic nanodendrites consisting of a dense array of Pt branches on a Pd core by reducing K_2PtCl_4 with L-ascorbic acid in the presence of uniform Pd nanocrystal seeds in an aqueous solution. The Pt branches supported on faceted Pd nanocrystals exhibited relatively large surface areas and particularly active facets toward the oxygen reduction reaction (ORR), the rate-determining step in a proton-exchange membrane fuel cell. The Pd-Pt nanodendrites were two and a half times more active on the basis of equivalent Pt mass for the ORR than the state-of-the-art Pt/C catalyst and five times more active than the first-generation supportless Pt-black catalyst.

Platinum (Pt) is the most effective catalyst to facilitate both hydrogen oxidation and oxygen reduction in a proton-exchange membrane (PEM) fuel cell (1–4), but several critical issues still need to be addressed before such cells can be commercialized for automotive applications: For example, the oxygen reduction reaction (ORR) is kinetically limited at the cathode (5–8), and the scale of the Pt crystallites leads to high costs for Pt-based electrocatalysts with sufficient surface area and activity (9). In order to overcome these barriers, it is necessary to maximize the activity of a Pt-based catalyst by engineering its morphology and/or composition.

During the last decade, a number of strategies have been proposed for improving the performance of an electrocatalyst for the ORR that involved alloying Pt with other transition metals at high temperatures (800 to 1000°C) (10, 11) or depositing a monolayer of Pt electrochemically onto fine particles of other metals immobilized on an electrode (12). Although these bimetallic catalysts have shown great improvements in activity, the lack of procedures for controlled large-scale synthesis has limited their use in commercial devices. In addition, the structural complexities of these systems have also made it difficult to decipher underlying mechanisms. For these reasons, the most commonly used electrocatalysts for the ORR are still based on fine particles of Pt supported on porous carbon materials (Pt/C). The catalytic activity of Pt nanoparticles can be drastically enhanced by maximizing the expression of certain facets that are intrinsically more active toward a specific reaction (13–16). However, it is rather difficult to synthesize Pt nano-

particles that combine both high surface area and the desired highly active facets on their surfaces because Pt nanoparticles of <5 nm in size tend to exist as truncated octahedrons cov-

ered by a mix of {100} and {111} facets in an effort to minimize the total interfacial free energy (16, 17).

Most recently, seeded growth has emerged for precisely controlling the morphology and composition of metallic nanostructures that are prepared using solution-phase methods (18–20). This technique has also enabled the preparation of bimetallic nanostructures with an unconventional morphology that cannot be achieved otherwise (20). Here we describe a facile, aqueous-phase route to synthesize bimetallic nanodendrites consisting of a dense array of Pt branches on a core of palladium (Pd) nanocrystal (NC). In this approach, truncated octahedral NCs of Pd with an average size of 9 nm were used as seeds so as to direct the dendritic growth of Pt upon the reduction of K_2PtCl_4 by L-ascorbic acid in an aqueous solution. Using this simple approach, we routinely produced Pd-Pt bimetallic nanodendrites with high surface areas and the particularly active facets for the ORR in high yields. These Pd-Pt nanodendrites displayed substantially enhanced ORR activity as compared with

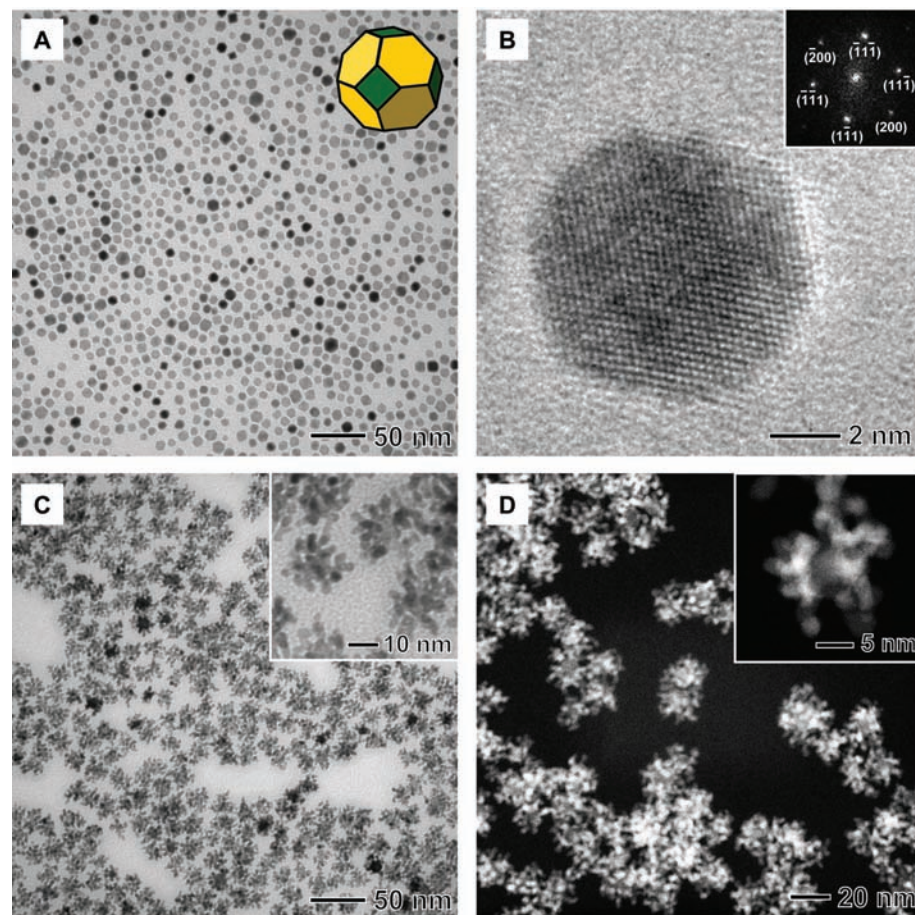


Fig. 1. (A) TEM image of truncated octahedral Pd NCs synthesized by reducing Na_2PdCl_4 with L-ascorbic acid in an aqueous solution. The inset shows a geometrical model of the truncated octahedron, where the green and yellow colors denote the {100} and {111} facets, respectively. (B) HRTEM image of a single truncated octahedron of Pd recorded along the [011] zone axis and the corresponding FT pattern (inset). (C) TEM image of Pd-Pt nanodendrites synthesized by reducing K_2PtCl_4 with L-ascorbic acid in the presence of truncated octahedral Pd NC seeds in an aqueous solution. (D) HAADF-STEM image of Pd-Pt nanodendrites.

¹Department of Biomedical Engineering, Washington University, St. Louis, MO 63130, USA. ²Department of Chemistry, Washington University, St. Louis, MO 63130, USA. ³Condensed Matter Physics and Materials Science Department, Brookhaven National Laboratory, Upton, NY 11973, USA.

*To whom correspondence should be addressed. E-mail: xia@biomed.wustl.edu

that of commercial Pt/C and Pt-black catalysts. This synthesis also provides a convenient and environmentally benign route to large-scale production because it does not require high temperature, organic solvent, or electrochemical deposition.

In the first step, we synthesized uniform, truncated octahedral NCs of Pd by reducing Na_2PdCl_4 with L-ascorbic acid in an aqueous solution (21). A transmission electron microscopy (TEM) image of the as-prepared Pd NCs is shown in Fig. 1A. The NCs were nearly 100% in truncated octahedral shape and had an average size of 9.1 nm (fig. S1) (21). A high-resolution TEM (HRTEM) image of a single Pd NC and the corresponding Fourier-transform (FT) pattern indicate that it was indeed a piece of single crystal with its surface being enclosed by both $\{111\}$ and $\{100\}$ facets (Fig. 1B). The fringe orientation in the HRTEM image also confirms its shape as a truncated octahedron encased by eight $\{111\}$ and six $\{100\}$ facets (fig. S2) (21).

These Pd NCs were then used as seeds for the formation of Pd-Pt bimetallic nanodendrites (21). A typical TEM image of the product revealed that a number of Pt branches had grown from a Pd core into dendritic tendrils, although single-arm branching was also observed (Fig. 1C). The Pd-Pt nanodendrites had an average size of 23.5 nm (fig. S3) (21). The energy-dispersive x-ray spectroscopy (EDS) line scanning analysis showed the bimetallic nanostructure consisting of a core rich in Pd and many arms rich in Pt (fig. S4) (21). The high-angle annular dark-field scanning TEM (HAADF-STEM) image in Fig. 1D shows the intense contrast between the core and the surrounding branches of a nanodendrite, demonstrating a three-dimensional dendritic morphology. Both TEM and STEM analyses confirmed the absence of isolated Pt nanoparticles in the product. The overall weight percentage of Pt in the Pd-Pt nanodendrites was 85% as determined by inductively coupled plasma mass spectrometry (ICP-MS) measurements.

We further characterized the Pd-Pt nanodendrites by means of HRTEM. Figure 2A gives an HRTEM image of a single Pd-Pt nanodendrite, which clearly shows overgrowth of Pt branches at multiple sites on the Pd seed. The nucleation sites for Pt appear to be distributed over the entire surface of the truncated octahedral Pd seed and do not overlap extensively. For the Pt branches, the average diameter was ~ 3 nm. The HRTEM image in Fig. 2B reveals the continuous lattice fringes from the Pd core to the Pt branches, indicating that the Pt branches were grown epitaxially on the Pd seed [Pd and Pt have a lattice mismatch of only 0.77% (20)]. HRTEM images of individual Pt branches (Fig. 2, C to F) show their single crystalline structure with a highly ordered continuous fringe pattern, and most of the exposed facets were found to be $\{111\}$, although some $\{110\}$ and high-index $\{311\}$ facets could also be identified in addition to a small fraction of $\{100\}$. The identical FT patterns associated with the same crystal orientations (Fig. 2, insets) are also indicative of the

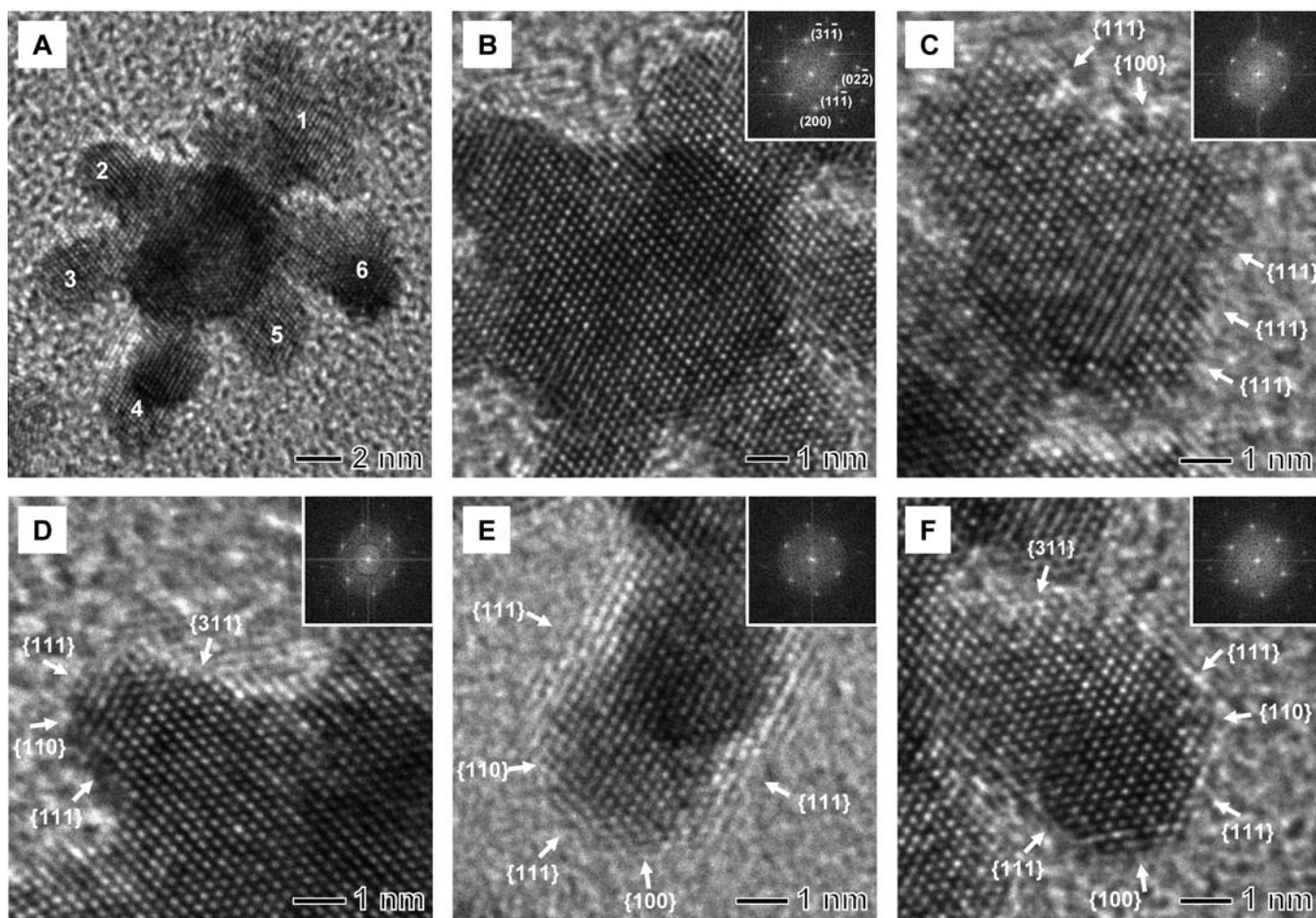


Fig. 2. (A) HRTEM image of a single Pd-Pt nanodendrite. (B) HRTEM image recorded from the center of the Pd-Pt nanodendrite shown in (A). The image clearly shows the continuous lattice fringes from the Pd core to the Pt branches, demonstrating the epitaxial relation between Pd and Pt. (C to F) HRTEM images recorded from Pt branches 1, 2, 4, and 6 marked in (A), respectively. The

images reveal that most of the exposed facets on the Pt branches were $\{111\}$ planes. Some $\{110\}$ and high-index $\{311\}$ facets can also be identified in addition to a small fraction of $\{100\}$ facets. The identical FT patterns shown in the insets indicate that the Pt branches have the same lattice orientation as the Pd core regardless of their different growth directions.

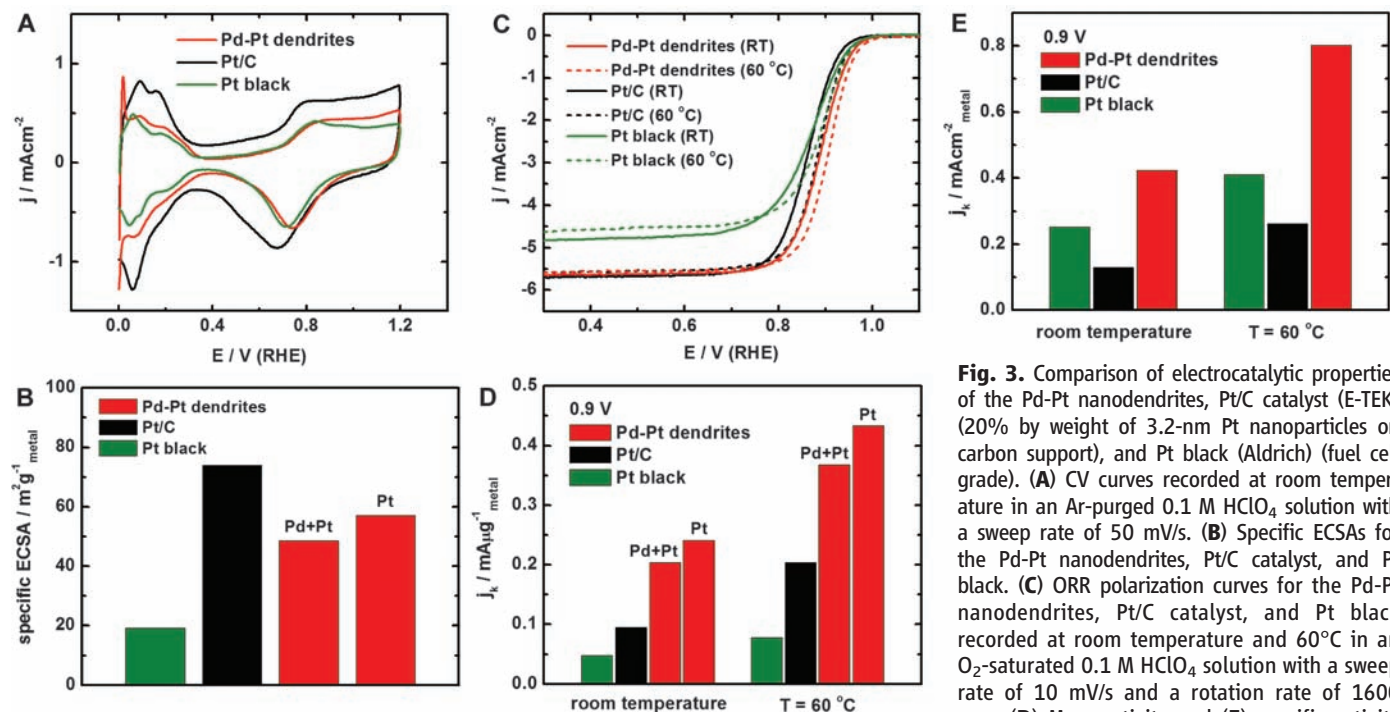


Fig. 3. Comparison of electrocatalytic properties of the Pd-Pt nanodendrites, Pt/C catalyst (E-TEK) (20% by weight of 3.2-nm Pt nanoparticles on carbon support), and Pt black (Aldrich) (fuel cell grade). (A) CV curves recorded at room temperature in an Ar-purged 0.1 M HClO₄ solution with a sweep rate of 50 mV/s. (B) Specific ECSAs for the Pd-Pt nanodendrites, Pt/C catalyst, and Pt black. (C) ORR polarization curves for the Pd-Pt nanodendrites, Pt/C catalyst, and Pt black recorded at room temperature and 60°C in an O₂-saturated 0.1 M HClO₄ solution with a sweep rate of 10 mV/s and a rotation rate of 1600 rpm. (D) Mass activity and (E) specific activity at 0.9 V versus RHE for these three catalysts. Mass and specific activities are given as kinetic current densities (j_k) normalized in reference to the loading amount and ECSA of metal, respectively. For the Pd-Pt nanodendrites or Pt/C catalyst, the metal loading on a RDE was 15.3 μg/cm², whereas the metal loading was 40.8 μg/cm² for the Pt black. In (A) and (C), current densities were normalized in reference to the geometric area of a RDE (0.196 cm²).

epitaxial relation between the Pd core and the Pt branches. The epitaxial overgrowth of single-crystal Pt branches suggests that they were formed via direct nucleation on the Pd NC seed rather than random aggregation of Pt nuclei that might be formed through homogeneous nucleation in the solution.

The observed dendritic growth of Pt branches can probably be attributed to the high rate of Pt reduction as mediated by an autocatalytic process (22), which has been used to account for the formation of porous and other branched nanostructures of Pt (23–26). In the present system, once Pt has nucleated on the surface of a Pd NC upon reduction by L-ascorbic acid, the Pt nuclei can serve as catalytic sites for further reduction of the Pt precursor and create favorable sites for atomic addition. Growth occurs preferentially on the Pt nuclei, and deposition proceeds along the developing Pt branches, rather than conformally on the Pd seed. We also observed branching via autocatalytic reduction of the Pt precursor in the absence of Pd seeds. In this case, however, the final product was dominated by a spherical, foamlike morphology with overall sizes of 20 to 35 nm (fig. S5) (21). This morphology might be caused by extensive overlap and possible fusion between adjacent branches during the growth process. The truncated octahedral Pd seeds provide multiple nucleation sites for Pt that are spatially separated from each other in order to avoid overlap and fusion and allow

the formation of Pt branches with an open dendritic structure.

We benchmarked the electrocatalytic properties of the Pd-Pt nanodendrites toward the ORR against both commercial Pt/C catalyst (E-TEK, Somerset, NJ) (20% by wt. of 3.2-nm Pt nanoparticles on Vulcan XC-72 carbon support) and Pt black (Aldrich, St. Louis, MO) (fuel cell grade). Figure 3A shows cyclic voltammetry (CV) curves of these three catalysts recorded at room temperature in Ar-purged 0.1 M HClO₄ solutions at a sweep rate of 50 mV/s. The CV curves exhibited two distinctive potential regions associated with H_{upd} adsorption/desorption processes ($H^+ + e^- = H_{upd}$) between $0 < E < 0.37$ V and the formation of a OH_{ad} layer ($2H_2O = OH_{ad} + H_3O^+ + e^-$) beyond ~0.6 V, where H_{upd} and OH_{ad} refer to the underpotentially deposited hydrogen and the adsorbed hydroxyl species, respectively. The electrochemically active surface area (ECSA) was calculated by measuring the charge collected in the H_{upd} adsorption/desorption region after double-layer correction and assuming a value of 210 μC/cm² for the adsorption of a hydrogen monolayer (21, 27). The specific ECSA (the ECSA per unit weight of metal) of the Pd-Pt nanodendrites (48.5 m²/g_{Pd+Pt}) was found to be 66% of the Pt/C catalyst (74.0 m²/g_{Pt}) (Fig. 3B). Based on the Pt mass, the specific ECSA of the Pd-Pt nanodendrites (57.1 m²/g_{Pt}) was 77% of the Pt/C catalyst. In contrast, the Pt black exhibited a small specific ECSA

(19.1 m²/g_{Pt}) mainly because of extensive agglomeration in the sample (fig. S6) (21). The highly branched structure of our Pd-Pt nanodendrites provides a reasonably high surface area despite their relatively large overall particle size.

The ORR measurements were performed in O₂-saturated 0.1 M HClO₄ solutions by using a glassy carbon rotating disk electrode (RDE) at both room temperature and 60°C. For the Pd-Pt nanodendrites and Pt/C catalyst, the metal loading on a RDE was 15.3 μg/cm², whereas the loading was increased to 40.8 μg/cm² for the Pt black so as to avoid a substantial drop of the diffusion-limiting currents that occurs at relatively low loadings for low-specific-surface-area catalysts (fig. S7) (21, 28). Polarization curves for the ORR on these three catalysts are shown in Fig. 3C. For all of these catalysts, the diffusion-limiting currents were obtained in the potential region below 0.6 V, whereas a mixed kinetic-diffusion control region occurs between 0.7 and 1.0 V. The kinetic current was calculated from the ORR polarization curve by using mass-transport correction and normalized to the loading amount of metal in order to compare the mass activity of different catalysts (21). At room temperature, the Pd-Pt nanodendrites exhibited a mass activity of 0.204 mA/μg_{Pd+Pt} on the basis of the total mass of Pd and Pt at 0.9 V versus a reversible hydrogen electrode (RHE), which was 2.1 and 4.3 times greater than that of the Pt/C

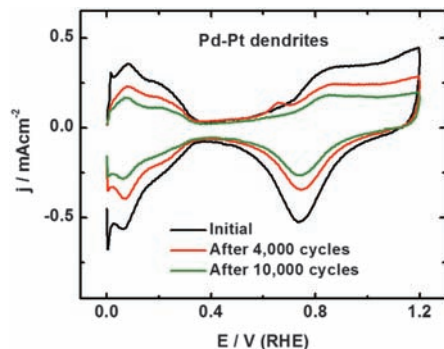


Fig. 4. CV curves for the Pd-Pt nanodendrites before and after accelerated durability test. The durability test was carried out for the same sample at room temperature in an O₂-saturated 0.1 M HClO₄ solution with the cyclic potential sweeping between 0.6 and 1.1 V at a sweep rate of 50 mV/s. The metal loading on a RDE was 15.3 μg/cm² and current densities were normalized in reference to the geometric area of a RDE (0.196 cm²).

catalyst (0.095 mA/μg_{Pt}) and the Pt black (0.048 mA/μg_{Pt}), respectively (Fig. 3D, left). If the Pt mass was solely taken into account, the mass activity of the Pd-Pt nanodendrites (0.241 mA/μg_{Pt}) was 2.5 times that of the state-of-the-art Pt/C catalyst for PEM fuel cells and 5.0 times that of the first-generation supportless Pt-black catalyst. At 60°C, the Pt mass activity of the Pd-Pt nanodendrites (0.433 mA/μg_{Pt}) was still greater than that of the Pt/C catalyst (0.204 mA/μg_{Pt}) and the Pt black (0.078 mA/μg_{Pt}) (Fig. 3D, right) and almost meets the performance targets for ORR fuel cell catalysts (0.44 mA/μg_{Pt} at 0.9 V versus RHE and 80°C) set by the U.S. Department of Energy (DOE) (9). In this study, the measured activities of the commercial Pt catalysts are in good agreement with the reported or predicted values in literature (9).

For a better understanding of the observed difference in ORR activity, we normalized the kinetic current against the ECSA of each catalyst. The Pd-Pt nanodendrites had a specific activity (i.e., kinetic current per unit surface area of catalyst) of 3.1 to 3.4 times that of the Pt/C catalyst and 1.7 to 2.0 times that of the Pt black depending on the temperature (Fig. 3E and table S1) (21), demonstrating the accelerated ORR kinetics on the surfaces of the Pd-Pt nanodendrites. The ORR activity on low-index crystallographic facets of Pt in a nonadsorbing electrolyte such as perchloric acid is known to increase on the order of Pt(100) << Pt(111) < Pt(110), with the difference in activity between Pt(111) and Pt(110) being minor (7, 29, 30). This difference in ORR activity most likely arises from the structure-sensitive inhibiting effect of OH_{ad} species on Pt(*hkl*), which blocks the active site for O₂ adsorption and thus retards the ORR kinetics. In addition, the high-index stepped Pt surfaces

have exhibited slightly greater ORR activities than the low-index planes in acidic solutions (31), which could be attributed to the favorable adsorption of O₂ molecules on the stepped surfaces (32, 33). The higher specific activity of the Pd-Pt nanodendrites might be related to the preferential exposure of {111} facets along with some {110} and high-index {311} facets on the Pt branches as compared with those of small Pt nanoparticles on Pt/C catalyst, which usually take the shape of a truncated octahedron and are thus enclosed by a mix of {100} and {111} facets (fig. S8) (21). As expected, the Pt black samples showed an irregular morphology with poorly defined facets. We can conclude that the observed high activity based on Pt mass for the Pd-Pt nanodendrites results from the reasonably high surface area intrinsic to the dendritic morphology and the exposure of particularly active facets toward the ORR on the Pt branches.

We also performed accelerated durability tests by applying linear potential sweeps between 0.6 and 1.1 V at 50 mV/s in O₂-saturated 0.1 M HClO₄ solutions at room temperature. After 4000 cycles, the CV measurements showed a loss of 30% in ECSA for the Pd-Pt nanodendrites, 36% for the Pt/C catalyst, and 33% for the Pt black (Fig. 4 and fig. S9) (21), suggesting that the Pd-Pt nanodendrites had durability slightly better than the Pt/C catalyst and the Pt black. After 10,000 cycles, the Pd-Pt nanodendrites showed a loss of 50% in ECSA. It might be possible to improve the durability of the Pd-Pt nanodendrites for the ORR by incorporating Au. Zhang *et al.* have recently demonstrated the stabilization of Pt ORR catalysts against Pt dissolution by modifying them with Au clusters, which were deposited onto the carbon-supported Pt nanoparticles through a galvanic replacement reaction (34). Their Au/Pt/C catalyst showed a negligible loss of 4% in ECSA after 30,000 cycles of the durability test. Additionally, enhancement of the ORR activity is expected through the optimization of both composition and dimension of the Pd-Pt nanodendrites by varying the ratio of Pt precursor to Pd seeds involved in a synthesis. By taking advantage of this controllable solution-phase synthesis, our approach provides a promising route to the development of next-generation catalysts with substantial reduction in Pt loading while retaining high ORR activity. The Pd-Pt bimetallic nanodendrites may also find use as catalysts beyond fuel cell applications.

References and Notes

1. T. E. Mallouk, *Nature* **343**, 515 (1990).
2. B. C. H. Steele, A. Heinzl, *Nature* **414**, 345 (2001).
3. M. L. Perry, T. F. Fuller, *J. Electrochem. Soc.* **149**, 559 (2002).
4. W. Vielstich, A. Lamm, H. A. Gasteiger, *Handbook of Fuel Cells: Fundamentals, Technology, and Applications* (Wiley, West Sussex, UK, ed. 1, 2003).

5. E. Yeager, *Electrochim. Acta* **29**, 1527 (1984).
6. N. M. Marković, T. J. Schmidt, V. Stamenković, P. N. Ross, *Fuel Cells (Weinh.)* **1**, 105 (2001).
7. N. M. Marković, P. N. Ross, *Surf. Sci. Rep.* **45**, 117 (2002).
8. W. Chen, J. Kim, S. Sun, S. Chen, *J. Phys. Chem. C* **112**, 3891 (2008).
9. H. A. Gasteiger, S. S. Kocha, B. Sompalli, F. T. Wagner, *Appl. Catal. B* **56**, 9 (2005).
10. S. Mukerjee, S. Srinivasan, *J. Electroanal. Chem.* **357**, 201 (1993).
11. S. Mukerjee, S. Srinivasan, M. P. Soriaga, J. McBreen, *J. Electrochem. Soc.* **142**, 1409 (1995).
12. R. R. Adzic *et al.*, *Top. Catal.* **46**, 249 (2007).
13. R. Narayanan, M. A. El-Sayed, *Nano Lett.* **4**, 1343 (2004).
14. N. Tian, Z.-Y. Zhou, S.-G. Sun, Y. Ding, Z. L. Wang, *Science* **316**, 732 (2007).
15. K. M. Bratlie, H. Lee, K. Komvopoulos, P. Yang, G. A. Somorjai, *Nano Lett.* **7**, 3097 (2007).
16. C. Wang, H. Daimon, T. Onodera, T. Koda, S. Sun, *Angew. Chem. Int. Ed.* **47**, 3588 (2008).
17. H. Song, F. Kim, S. Connor, G. A. Somorjai, P. Yang, *J. Phys. Chem. B* **109**, 188 (2005).
18. S. E. Habas, H. Lee, V. Radmilovic, G. A. Somorjai, P. Yang, *Nat. Mater.* **6**, 692 (2007).
19. H. Lee, S. E. Habas, G. A. Somorjai, P. Yang, *J. Am. Chem. Soc.* **130**, 5406 (2008).
20. B. Lim *et al.*, *Nano Lett.* **8**, 2535 (2008).
21. Materials and methods are available as supporting material on Science Online.
22. L. C. Ciacchi, W. Pompe, A. D. Vita, *J. Phys. Chem. B* **107**, 1755 (2003).
23. Y. Song *et al.*, *J. Am. Chem. Soc.* **126**, 635 (2004).
24. J. Chen, T. Herricks, Y. Xia, *Angew. Chem. Int. Ed.* **44**, 2589 (2005).
25. X. Teng, X. Liang, S. Maksimuk, H. Yang, *Small* **2**, 249 (2006).
26. B. Lim *et al.*, *Nano Lett.* **8**, 4043 (2008).
27. T. J. Schmidt *et al.*, *J. Electrochem. Soc.* **145**, 2354 (1998).
28. K. J. J. Mayrhofer *et al.*, *Electrochim. Acta* **53**, 3181 (2008).
29. N. Markovic, H. Gasteiger, P. N. Ross, *J. Electrochem. Soc.* **144**, 1591 (1997).
30. V. R. Stamenkovic *et al.*, *Science* **315**, 493 (2007).
31. A. Kuzume, E. Herrero, J. M. Feliu, *J. Electroanal. Chem.* **599**, 333 (2007).
32. D. W. Blakely, G. A. Somorjai, *Surf. Sci.* **65**, 419 (1977).
33. N. M. Marković, R. R. Adzic, B. D. Cahan, E. B. Yeager, *J. Electroanal. Chem.* **377**, 249 (1994).
34. J. Zhang, K. Sasaki, E. Sutter, R. R. Adzic, *Science* **315**, 220 (2007).
35. This work was supported by startup funds from Washington University in St. Louis. B.L. was also partially supported by postdoctoral fellowships from the Korea Research Foundation funded by the Korean Government (KRF-2006-352-D00067). P.H.C.C. was also supported in part by the Fulbright Program and the Brazilian Ministry of Education (Coordenação de Aperfeiçoamento de Pessoal de Nível Superior). E.C.C. was also partially supported by postdoctoral fellowships from the Korea Research Foundation funded by the Korean Government (KRF-2007-357-D00070). J.T. and Y.Z. were supported by the U.S. DOE/Basic Energy Sciences (DEAC02-98CH10886). We thank H. Yang for technical assistance with the electrochemical measurements.

Supporting Online Material

www.sciencemag.org/cgi/content/full/1170377/DC1
Materials and Methods
Figs. S1 to S9
Table S1

30 December 2008; accepted 9 April 2009
Published online 14 May 2009;
10.1126/science.1170377
Include this information when citing this paper.

Pd-Pt Bimetallic Nanodendrites with High Activity for Oxygen Reduction

Byungkwon Lim, Majjong Jiang, Pedro H. C. Camargo, Eun Chul Cho, Jing Tao, Xianmao Lu, Yimei Zhu and Younan Xia

Science **324** (5932), 1302-1305.

DOI: 10.1126/science.1170377 originally published online May 14, 2009

Extending Platinum Catalysts

Platinum performs extremely well as a catalyst for the oxygen-reduction reaction that runs under highly acidic conditions in proton-exchange membrane fuel cells, but is expensive. One strategy for reducing costs is to increase the surface area of the platinum. **Lim *et al.*** (p. 1302, published online 14 May) describe a simple chemical route, in which Pt ions in solution are reduced onto Pd seed crystals, which creates faceted Pt nanocrystals with a high area owing to their dendritic architecture. On a Pt mass basis, these catalysts are several times more active than conventional Pt catalysts.

ARTICLE TOOLS

<http://science.sciencemag.org/content/324/5932/1302>

SUPPLEMENTARY MATERIALS

<http://science.sciencemag.org/content/suppl/2009/05/14/1170377.DC1>

REFERENCES

This article cites 32 articles, 3 of which you can access for free
<http://science.sciencemag.org/content/324/5932/1302#BIBL>

PERMISSIONS

<http://www.sciencemag.org/help/reprints-and-permissions>

Use of this article is subject to the [Terms of Service](#)